# Towards $^{99m}$Tc- and Re-Based Multifunctional Silica Platforms for Theranostic Applications

**Michel A. Wuillemin [1], Michael J. Reber [2], Thomas Fox [1], Bernhard Spingler [1], Dominik Brühwiler [2], Roger Alberto [1] and Henrik Braband [1,***

[1]  Department of Chemistry, University of Zurich, Winterthurerstr. 190, CH-8057 Zurich, Switzerland; michel.wuillemin@gmx.ch (M.A.W.); thomas.fox@chem.uzh.ch (T.F.); spingler@chem.uzh.ch (B.S.); ariel@chem.uzh.ch (R.A.)
[2]  Institute of Chemistry and Biotechnology, Zurich University of Applied Sciences, Einsiedlerstrasse 31, 8820 Wädenswil, Switzerland; michaelreber1@gmail.com (M.J.R.); breh@zhaw.ch (D.B.)
*   Correspondence: henrik.braband@chem.uzh.ch

**Abstract:** Taking advantage of the radiation properties of $^{99m}$Tc and $^{186/188}$Re and the photophysical characteristics of the $\{M(CO)_3\}^+$ moiety (M = Re), we developed a multifunctional silica platform with the theranostic pair $^{99m}$Tc/Re with high potential for (nano)medical applications. Starting with a general screening to evaluate the most suitable mesoporous silica construct and the development of appropriate chelate systems, multifunctional mesoporous silica microparticles (SBA-15) were synthesized. These particles act as a model towards the synthesis of the corresponding nanoconstructs. The particles can be modified at the external surface with a targeting function and labeled with the $\{M(CO)_3\}^+$ moiety (M = $^{99m}$Tc, Re) at the pore surface. Thus, a silica platform is realized, whose bioprofile is not altered by the loaded modalities. The described synthetic procedures can be applied to establish a target-specific theranostic nanoplatform, which enables the combination of fluorescence and radio imaging, with the possibility of radio- and chemotherapy.

**Keywords:** technetium; rhenium; complexes; mesoporous silica; MCM-41; SBA-15; theranostic; multimodality; radioprobe

## 1. Introduction

For many decades, the nuclear isomer technetium-99m ($^{99m}$Tc, $t_{1/2}$ = 6 h, $E_\gamma$ = 141 keV) has been the most frequently used radio metal for applications in nuclear medical diagnostics [1–5]. In combination with isotopes 186 and 188 of its heavier homolog rhenium ($^{186/188}$Re), it represents one of the first "theranostic pairs" for nuclear medical diagnosis and therapy [6]. Recently, a conceptual extension of the "theranostic pair" Tc/Re was described by the combination of a $^{99m}$Tc-based bio-mimetic with its organometallic but non-radioactive rhenium homologue [7]. The rhenium complex should be therapeutically active through its structure, while the $^{99m}$Tc homologue allows for visualizing the pharmacology. Besides the use of Tc and Re as a "theranostic pair", Stephenson et al. demonstrated that the two homologues allow the development of multimodal imaging probes [8]. A fluorescent Re-complex and the analogous $^{99m}$Tc-complex provide the direct combination of optical imaging with high spatial resolution (in vitro) and radioimaging with sensitive detection of biological processes deep in the body (in vivo). By combining the multimodality of the $\{M(CO)_3\}^+$ moiety (M = $^{99m}$Tc, Re) with the theranostic properties of the $^{99m}$Tc/$^{186/188}$Re pair, a multifunctional system is realized, which can be applied for diagnosis (radio and UV imaging) and (radio) therapy. This represents a new strategy for the application of Tc and Re in medicine and will enable new opportunities for these two elements. To apply multimodality probes in medicine, they have to be target-specific. To design a target-specific molecular

scaffold that combines all of the described Tc/Re-based modalities is challenging. Attractive alternatives are target-specific mesoporous nanoplatforms, which can incorporate the different modalities. An advantage of this approach is that the bioprofile of the target-specific mesoporous nanoplatform is not altered by the incorporated modality (Figure 1).
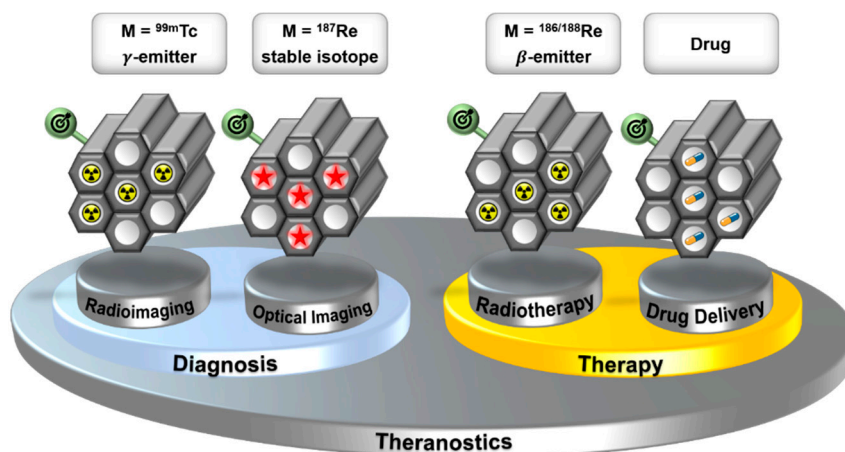


**Figure 1.** Target-specific mesoporous silica (nano)particles as a multifunctional platform, using the "theranostic pair" Tc/Re. The incorporated modalities can be changed without altering the bioprofile of the construct.

Currently, multifunctional nanoplatforms are a focus in nanomedicine [9]. Nanoparticles are ideal for combining different modalities and exhibit several advantages as compared to traditional diagnostic and therapeutic methods. They can easily integrate more than one kind of imaging or therapeutic agent. Large amounts of imaging agents or drugs can be introduced through chemical conjugation or simple loading due to the large surface area or interior cargo volume of the nanoparticles. Moreover, nanoparticles can target disease sites for drug delivery and imaging through physicochemical optimization of size and surface properties, and especially through the attachment of specific targeting moieties. Alteration of physicochemical properties can also be used to optimize the circulation time in the blood [10]. A further interesting feature of nanoparticles in radiopharmacy is the possibility to accumulate more than one radioactive moiety per target receptor. This leads to higher activity at the target site (amplification effect) as compared to directly labeled targeting molecules, which can only deliver one radioactive moiety per target receptor [11]. These beneficial properties of nanoparticles lead to a better contrast of the diagnostic image. The overall radioactivity can be reduced, leading to lower dose rates for the patients. In the past, different nanomaterials have been labeled with $^{99m}$Tc in a nonspecific fashion, such as magnetic nanoparticles [12–15], organo-germanium compounds [16], carbon nanotubes [17], fullerene derivatives [18], polymers [19], pullulan acetates [20], chitosans [21,22], and tripalmitins [23]. In all these approaches, $[^{99m}TcO_4]^-$ activity has been reduced in the presence of the nanoparticles. This leads to a random distribution of $^{99m}$Tc at the surface of the nanoparticles and an undefined binding mode at the particle surface. This unspecific labeling method is fast, but unambiguous characterization of the labeled nanoparticles is challenging. For the preparation of well-defined mesoporous nanoparticles, whose external and pore surface can be addressed independently at different stages of the synthesis, a specific and reproducible method to bind technetium and rhenium is required. Furthermore, developing a well-defined labeling procedure for nanoparticles with $^{99m}$Tc can serve as a useful tool to investigate general aspects of nanoparticles, such as entry routes, pharmacokinetics, and the molecular mechanism of nanoparticle toxicity [24].

Mesoporous silica particles show highly interesting properties that make them promising candidates for target-specific, multifunctional nanoplatforms (Figure 1). Especially, selective functionalization of the external and the pore surface area as well as cargo loading are established features for this type of material [25–29]. Besides applications in catalysis [30–35] and sensing [36], MCM-41 (Mobil Composition

of Matter No. 41), a prominent representative of mesoporous silica particles, was first proposed as a drug delivery system in 2001 [37]. Since then, extensive research efforts have been dedicated to this subject, leading to sophisticated systems for drug delivery and controlled drug release [38–43]. Therefore, mesoporous silica particles enable the development of carrier systems, which combine targeting moieties, Tc- and Re-based imaging functions (radio- or UV-labels), and drug loading in a well-defined way. This creates multifunctional nanoplatforms, which are extremely suited for future applications in the evolving field of nanomedicine and personalized medicine [44].

Herein, we describe the development of a Tc and Re based multifunctional silica microplatform. This platform acts as a model towards the synthesis of the corresponding nanoconstructs. Starting with a general screening of different mesoporous silica microparticles to evaluate the most suitable construct and the development of appropriate chelate systems, multifunctional mesoporous silica particles, such as SBA-15 (Santa Barbara Amorphous type material No. 15) and spherical SBA-15 (sSBA-15), are synthesized. These particles can be labeled with the $\{M(CO)_3\}^+$ moiety (M = $^{99m}$Tc, Re) at the pore surface.

## 2. Results and Discussion

### 2.1. Evaluation of Mesoporous Silica Particles

The term mesoporous silica represents a large family of compounds with a plethora of properties. To understand which type of mesoporous silica particle is suitable as a theranostic platform, in a first step a variety of different types of mesoporous silica microparticles, such as MCM-41 (Mobil Composition of Matter No. 41) [45], ASNCs (arrays of silica nanochannels) [46], and SBA-15 (Santa Barbara Amorphous type material No. 15) [47] were evaluated (for details see Supplementary Materials). All studied materials are established mesoporous silica microparticles. The screening was done by comparing the labeling performance of the functionalized silica microparticles, applying a new $^{99m}$Tc labeling strategy [48,49]. The (3 + 2)-cycloaddition reaction of the $[^{99m}TcO_3(tacn)]^+$ complex (tacn = 1,3,5-triazacacyclononane) with surface-grafted norbornene proceeds stereoselectively and with high reaction rates [50]. Therefore, it is an excellent method for fast and efficient screening of different materials. For this screening, 5-(bicycloheptenyl)triethoxysilane (NorboSi) was grafted to the surfaces of the silica particles under study in the first step. In the second step, $[^{99m}TcO_3(tacn)]^+$ was reacted with these modified particles. Progress of labeling can be monitored by the decrease of the activity in the solution over time. Furthermore, the labeled particles were decomposed in 1M NaOH as control and the released activity was correlated to the observed decrease of activity in the solution by radio-HPLC. Figure 2 shows the labeling progress for two representative examples of the studied microparticles (MCM-41 and SBA-15).
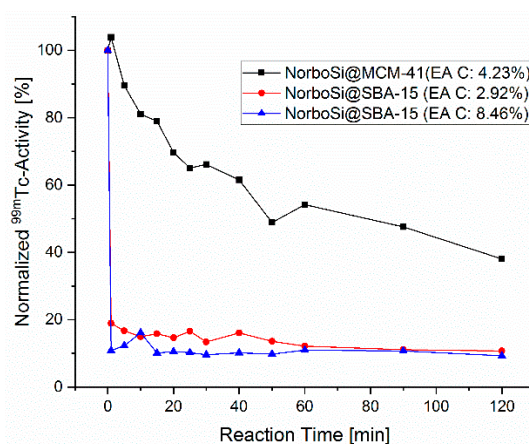


**Figure 2.** Labeling of NorboSi modified silica particles, NorboSi@MCM-41 (black), NorboSi@SBA-15 with low loading of functional groups (red), and NorboSi@SBA-15, with a high loading of functional

groups (blue). Percentages in brackets represent the carbon content of these particles, determined by elemental analysis (EA C). Conditions: 10 mg NorboSi modified silica particles suspended in 2 mL saline solution, addition of 2 mL $[^{99m}TcO_3(tacn)]^+$ solution, sonication for 2 h, start temperature 25 °C (increased to 40 °C over the reaction time of 2 h).

The screening disclosed a remarkable difference in the labeling performance of the modified silica particles depending on the porosity. Whereas SBA-15 particles showed very fast and almost complete labeling (more than 90% labeling yield in less than 1 min reaction time), the MCM-41 particles had a much slower labeling rate. After 2 h reaction time, a labeling yield of only 60% was observed. Analysis of the gained data of all studied materials shows that silica particles with more accessible surface area lead to higher rates for the $^{99m}Tc$-labeling. For mesoporous silica microparticles, most of the surface area (roughly 90%) is located in the pores. A larger pore diameter gives enhanced access for $[^{99m}TcO_3(tacn)]^+$ to the norbornene decorated pores. As a consequence, particles with larger average pore size, such as SBA-15 (7–7.5 nm), show superior labeling performance as compared to particles with significantly smaller average pore size, such as MCM-41 (4 nm). The amount of grafted norbornenesilane (as determined by elemental analysis) has no significant influence as compared to the much more crucial pore size and accessible surface area. Due to the outstanding labeling performance of SBA-15 microparticles in contrast to all other tested silica particles, only this class of particles was considered for further investigation. In contrast to the synthetic procedure for SBA-15 microparticles, no synthetic procedures for well-defined SBA-15 nanoparticles are established. However, we expect that the herein reported procedures for the synthesis of bifunctionalized SBA-15 microparticles can be applied without further modifications for the synthesis of a SBA-15-based theranostic nanoplatform.

*2.2. Synthesis of Chelators for Surface Modifications*

By applying the (3 + 2)-cycloaddition $[^{99m}TcO_3(tacn)]^+$ with alkenes, an efficient new method was established to study the accessibility of functional groups (NorboSi) at silica particle surfaces. However, the high-valent chemistry of the $\{^{99m}TcO_3\}^+$ was not established for theranostic applications due to the different redox potentials of the elements Tc and Re at their highest oxidation states [48]. This would limit a potential target-specific NorboSi@SBA-15 construct to radioimaging with $^{99m}Tc$ and conventional drug loading, disregarding the full potential of the theranostic pair $^{99m}Tc/Re$. Therefore, an alternative approach with the $\{M(CO)_3\}^+$ core (M = Re, $^{99m}Tc$) and SBA-15 particles was selected. For the development of theranostic nanoplatforms for (nuclear) medical applications, the bisquinoline/$\{M(CO)_3\}^+$ (M = Re, $^{99m}Tc$) system is very well suited. The correlation of radioimaging and fluorescence studies with this system in single amino acid chelates was reported by Stephenson et al. [8]. SBA-15 particles carrying tridentate bisquinoline ligands enable the coordination of $\{^{99m}Tc(CO)_3\}^+$ for radioimaging, $\{^{185/187}Re(CO)_3\}^+$ for optical imaging, and $\{^{186/188}Re(CO)_3\}^+$ for radiotherapy. Aiming at the synthesis of SBA-15 particles carrying bisquinoline chelates, a successive synthesis of the bisquinoline moiety (first by grafting of aminoalkyltriethoxysilane, followed by reductive amination with 2-quinolinecarboxaldehyde) at the SBA-15 surface is attractive. However, previous studies have shown that for this particular chelate, such a synthetic procedure does not lead to well-defined particles but generates a mixture of bi- and tridentate chelates at the silica surface [51]. Therefore, functionalization of SBA-15 by grafting of bisquinoline trialkoxysilanes is preferred. Different bisquinoline moieties with appropriate terminal substituents for the attachment of trialkoxysilanes have been synthesized (Scheme 1) in direct reductive amination.
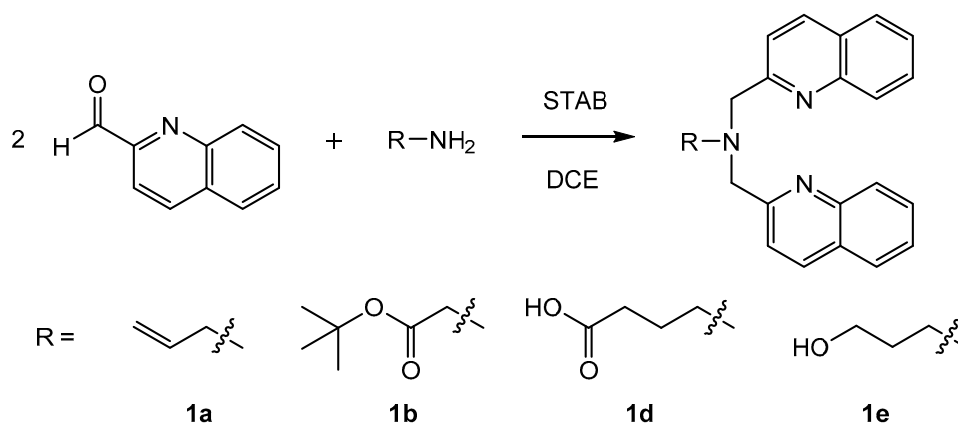
**Scheme 1.** Synthesis of different bisquinoline moieties with appropriate terminal substituents for the attachment of trialkoxysilanes. Reaction time was 2–25 h at room temperature. Note: STAB = sodium triacetoxyborohydride; DCE = 1,2-dichloroethane.

All compounds were isolated and characterized (see Supplementary Materials). The carboxyl group was introduced into the bisquinoline moiety by a one-step reaction with 4-aminobutyric acid (**1d**) or in a two-step procedure via deprotection of **1b** (Scheme 2).
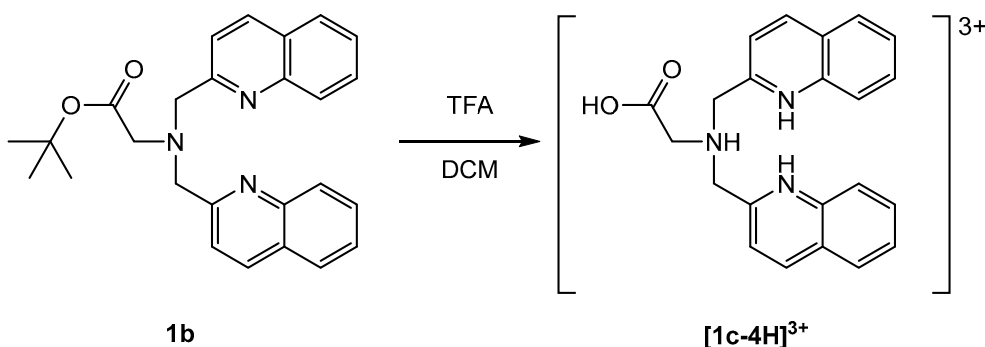


**Scheme 2.** Deprotection of **1b** with TFA via microwave reaction for 20 min at 90 °C. Note: TFA = trifluoroacetic acid; DCM = dichloromethane.

The elemental composition of **[1c-4H](TFA)₃** suggested the formation of a three-fold positively charged cation (**[1c-4H]³⁺**). Single crystals of **[1c-3H]Cl(TFA)·(HTFA)** were obtained by slow evaporation of a CDCl₃ solution of **[1c-4H](TFA)₃** (Figure 3). The chloride anion obviously originated from the solvent. In the structure of **[1c-3H]Cl(TFA)·(HTFA)**, two trifluoroacetic acid (TFA) anions share one proton. The two quinoline nitrogen atoms are protonated and both form hydrogen bonds with a common chloride anion (3.2019 (14) Å). In this structure, a TFA molecule is protonated, while the aliphatic tertiary amine is not (for crystallographic details see Supplementary Materials). This finding is in contrast with the expected pKa values of TFA and amines in solution. This rare structural motif of doubly-protonated pyridine rings pointing to a common hydrogen acceptor despite the presence of the more basic aliphatic nitrogen of the bispicolylamine has been described before [52,53].
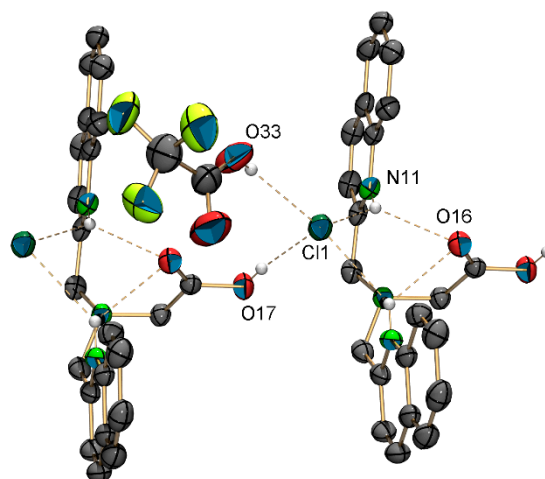
Symmetry operation: *x* + 1, *y*, *z*.

**Figure 3.** ORTEP representation [54] of the crystal packing of **[1c-3H]Cl(TFA)·(HTFA)**, showing the important hydrogen bonds. Thermal ellipsoids represent 50% probability. One TFA anion and hydrogen atoms that are not involved in hydrogen bonds are omitted for clarity. Selected hydrogen bonds (D···A) [Å]: O17–Cl1 2.9763 (19), O33–Cl1 2.993 (4), N11–Cl1[*] 3.2019(14), N11–O16 3.0084 (17).

Positive electron density between the trifluoroacetate molecule and the chloride anion indicates that the TFA is protonated and forms a hydrogen bond with the chloride anion (O33–Cl1: 2.993 (4) Å). The distance of this hydrogen bond is typical for such carboxylic acid–chloride interactions [55]. The overall crystal packing and the local environment of two pyridinium units next to the amine and one chloride ion next to the TFA are all responsible for this rare structural feature.

The synthesized chelates can be coupled to trialkoxysilanes via hydrosilylation and cross-metathesis (**1a**), amide bond formation (**1c, 1d**), or substitution reactions (**1e**). The amide bond formation of 3-aminopropyltriethoxysilane (APTES) with the acid bisquinoline moiety **1d** is the most efficient synthetic approach (Scheme 3).
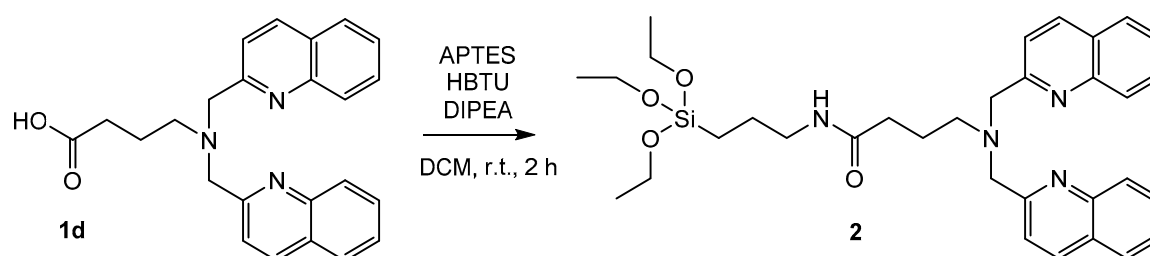


**Scheme 3.** Synthesis of **2** by amide bond formation of **1d** with 3-aminopropyltriethoxysilane (APTES) for 2 h at room temperature. Note: HBTU = 2-(1H-Benzotriazol-1-yl)-1,1,3,3-tetramethyluronium-hexafluorophosphate; DIPEA = *N,N*-Diisopropylethylamine.

The amide bond formation of APTES with a carboxylic acid represents a general strategy for the synthesis of functionalized trialkoxysilanes. It is fast and work up procedures are efficient. Extraction with dichloromethane (DCM) is sufficient to obtain the product in high purity. Tetramethylurea, the only side product, does not interfere with the subsequent grafting onto silica particles. As an alternative, the direct reductive amination of 2-quinolinecarboxaldehyde with APTES is a direct and efficient synthetic pathway (Scheme 4).

The ethoxysilane groups tend to hydrolyze and subsequently cross-link. This undesired side reaction has been addressed with EtOH for quenching of the residual reducing agent and C-18 flash chromatography purification. The isolated bisquinolinepropyltriethoxysilane (**3**) is stable as a solid

under ambient conditions over a period of several months. To evaluate the optimal reaction condition for the bifunctionalization of SBA-15 particles, compound **3** was grafted in high (160 M) and low (4 M) concentrations onto SBA-15 particles in dry toluene (Scheme 4).
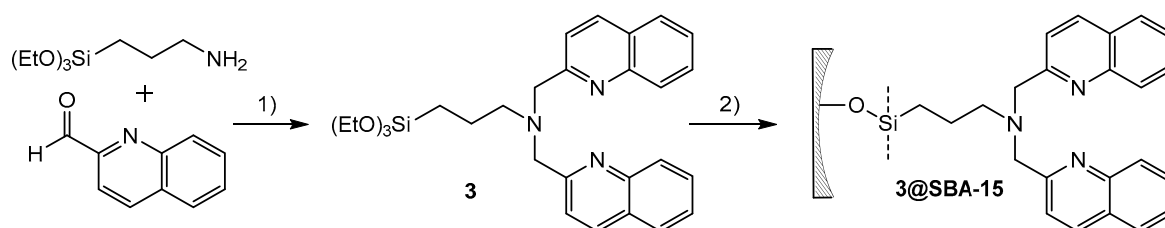


**Scheme 4.** Synthesis of **3** by reductive amination of 2-quinolinecarboxaldehyde with 3-aminopropyltriethoxysilane in the presence of sodium triacetoxyborohydride (3.5 h, room temperature). Subsequent grafting of **3** to SBA-15 particles (2 h sonication, 60 °C).

The intact porous network of the modified SBA-15 particles (**3@SBA-15**) and successful grafting to the external surface as well as to the pore surface was confirmed by determining the decrease of the pore volume, the average pore diameter, and the total specific surface area (Table 1).

**Table 1.** $N_2$-sorption values for SBA-15 and **3@SBA-15** particles, which contain 0.37 mmol **3**/g particles (determined by elemental analysis).

| Particles | Average Pore Size [nm] | Total Pore Volume [$cm^3$/g] | BET Surface Area [$m^2$/g] |
|---|---|---|---|
| **SBA-15** | 7.0 | 0.75 | 570 |
| **3@SBA-15** | 6.8 | 0.64 | 441 |

The integrity of the grafted **3** was shown by decomposing the particles in 1M NaOD in $D_2O$ and subsequent analysis of the solution by ^{1}H-NMR and HR-ESI MS (high resolution-electrospray ionization mass spectrometry); an analytical strategy that was recently developed by Farinha and coworkers [56]. HR-ESI and ^{1}H-NMR allowed for unambiguous characterization of the hydrolyzed form of **3** and showed the release of EtOD due to the hydrolysis of Si–OEt groups not involved in the binding to SBA-15. Quantification of the **3@SBA-15** particles with high **3** content by elemental analysis showed 0.37 mmol of **3** per g of SBA-15, which correlates to 0.33 molecules of **3** per $nm^2$ surface of SBA-15. For comparison, applying **3** in lower concentrations for the synthesis led to **3@SBA-15** particles containing 0.08 mmol **3** per g particles.

Since **3** is highly stable, an alternative method for the synthesis of **3@SBA-15** is the co-condensation approach. This led to microparticles showing high loading and homogeneous distribution of the functionality over the complete porous network. Detailed synthetic procedures for all syntheses are described in the supplementary.

## 2.3. Reactions of Bisquinoline Molecules with the {$M(CO)_3$}$^+$ Moiety (M = Re, $^{99m}$Tc)

The chelates **1a**, **1b, 1e**, and **3** were reacted with $(NEt_4)_2[ReBr_3(CO)_3]$ and the products $[(\mathbf{1a})Re(CO)_3]^+$, $[(\mathbf{1b})Re(CO)_3]^+$, $[(\mathbf{1e})Re(CO)_3]^+$, and $[(\mathbf{3})Re(CO)_3]^+$ (**3-Re**) were isolated and fully characterized. Single crystals, suitable for X-ray diffraction analysis, were obtained for $[(\mathbf{1a})Re(CO)_3](PF_6)$, $[(\mathbf{1b})Re(CO)_3](PF_6)$ and $[(\mathbf{1e})Re(CO)_3](PF_6)$ by vapor diffusion (Figure 4).

Furthermore, the photophysical properties of **3-Re** were studied. The UV–Vis spectrum of **3-Re** shows a maximum absorbance at 323 nm with an extinction coefficient of 13696 $M^{-1} \cdot cm^{-1}$ in $CHCl_3$ under ambient conditions. The emission spectrum shows two distinct emissions at 426 and 546 nm. These data are in good agreement with Stephenson et al [8]. Under an inert gas atmosphere ($N_2$), two emission maxima at 383 and 566 nm can be observed. The lifetime of the excited state determined in

$CHCl_3/N_2$ is 12.5 µs. This is long enough to enable time-gating techniques, which are necessary to overcome interferences from endogenous fluorescence during in vitro imaging studies [8].
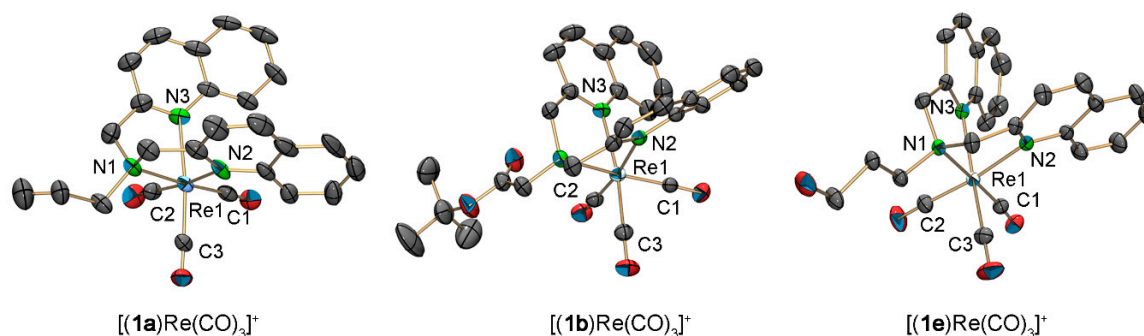


$[(\mathbf{1a})Re(CO)_3]^+$　　　　　　　$[(\mathbf{1b})Re(CO)_3]^+$　　　　　　　$[(\mathbf{1e})Re(CO)_3]^+$

**Figure 4.** ORTEP representation [54] of the $[(\mathbf{1a})Re(CO)_3]^+$, $[(\mathbf{1b})Re(CO)_3]^+$, and $[(\mathbf{1e})Re(CO)_3]^+$ cations of the crystal structure of $[(\mathbf{1a})Re(CO)_3](PF_6)$, $[(\mathbf{1b})Re(CO)_3](PF_6)$, and $[(\mathbf{1e})Re(CO)_3](PF_6)$. Thermal ellipsoids represent 50% probability. Hydrogen atoms are omitted for clarity. Selected bond lengths [Å] and angles [°]: $[(\mathbf{1a})Re(CO)_3](PF_6)$, Re1–C1 1.899 (5), Re1–C2 1.925 (5), Re1–C3 1.909 (5), Re1–N1 2.199 (5), Re1–N2 2.218 (4), Re1–N3 2.207 (4), C1–Re1–C2 86.7 (2), C1–Re–C3 83.1 (2), N1–Re1–N2 75.70 (16), N1–Re1–N3 79.49 (19); $[(\mathbf{1b})Re(CO)_3](PF_6)$, Re1–C1 1.915 (4), Re1–C2 1.918 (4), Re1–C3 1.927 (4), Re1–N1 2.230 (3), Re1–N2 2.224 (3), Re1–N3 2.216 (3), C1–Re1–C2 88.94 (16), C1–Re–C3 84.06 (15), N1–Re1–N2 73.64 (11), N1–Re1–N3 78.71 (11); $[(\mathbf{1e})Re(CO)_3](PF_6)$, Re1–C1 1.909 (2), Re1–C2 1.920 (3), Re1–C3 1.914 (3), Re1–N1 2.2282 (17), Re1–N2 2.2391 (18), Re1–N3 2.2164 (18), C1–Re1–C2 83.09 (10), C1–Re–C3 84.93 (10), N1–Re1–N2 77.14 (7), N1–Re1–N3 78.61 (7).

Grafting of **3-Re** onto SBA-15 particles or solid phase supported reaction of **3@SBA-15** with $[Re(H_2O)_3(CO)_3]^+$ results in **3-Re@SBA-15** particles (Scheme 5). HPLC of the reaction solution of the reaction of **3-Re** with SBA-15 particles (route a)) did not show any release of $[Re(H_2O)_3(CO)_3]^+$. Therefore, it can be assumed that this reaction yields **3-Re@SBA-15** particles, which do not contain uncoordinated **3**. This was confirmed by the addition of $[^{99m}Tc(H_2O)_3(CO)_3]^+$ to these particles, which did not lead to a labeling of the particles. However, in the context of potential nuclearmedical applications, synthetic route a) would require a two-step procedure, starting with the synthesis of **3-$^{186/188}$Re**, followed by the grafting process. The increased complexity of this synthetic procedure reduces its potential for clinic applications. From a theranostic point of view, the second approach (synthetic route b)) has higher relevance due to a one-step labeling procedure. Aiming to establish a feasible labeling for medical applications with the radio isotopes $^{186/188}$Re and $^{99m}$Tc, $[Re(H_2O)_3(CO)_3]^+$ was chosen as a precursor for these reactions. In contrast to $[Re(Br)_3(CO)_3]^+$, this precursor allows for a direct translation of the model reaction with $[Re(H_2O)_3(CO)_3]^+$ into a labeling procedure with $[^{186/188}Re(H_2O)_3(CO)_3]^+$ and $[^{99m}Tc(H_2O)_3(CO)_3]^+$. Labeling of **3@SBA-15** particles, which contained 0.08 mmol **3**/g particles (determined by EA) with an excess of $[Re(H_2O)_3(CO)_3]^+$, yielded **3-Re@SBA-15** particles with an Re loading of 0.077 mmol/g particles (determined by ICP-MS). The incomplete occupation of the bisquinoline ligands at the surface of these fluorescent **3-Re@SBA-15** particles allows for subsequent labeling with $[^{99m}Tc(H_2O)_3(CO)_3]^+$ in a second step (detail see Supplementary Figure S4.4.3). For both synthetic routes, the CO bands in the IR spectrum clearly indicate successful coordination of the $\{Re(CO)_3\}^+$ core (Figure 5). The CO vibrations of **3-Re@SBA-15** (2026, 1901, and 1981 $cm^{-1}$) are in good agreement with the vibrations found for the **3-Re** (2025 and 1901 $cm^{-1}$, Supplementary Figure S4.2.4.1). For comparison, the CO vibrations of the precursor complexes $[ReBr_3(CO)_3]^{2-}$ and $[Re(H_2O)_3(CO)_3]^+$ can be observed at 1997 and 1844, and 2037 and 1916 $cm^{-1}$, respectively [57]. The intensive bands at 1043 $cm^{-1}$ can be assigned to Si–O vibrations of the bulk material.

The labeling of **3@SBA-15** with $[^{99m}Tc(H_2O)_3(CO)_3]^+$ (Scheme 5, synthetic route b)) to yield **3-$^{99m}$Tc@SBA-15** was fast, with a labeling yield > 99%. Detailed information for this labeling procedure can be found in the Supplementary Materials (Supplementary Figure S4.3.4). As for the screening of different silica materials, the labeling progress was indirectly analyzed by determining the decrease

of activity in the solution. Prior to the reaction, radio-HPLC of the solution shows a clear signal for the $[^{99m}Tc(H_2O)_3(CO)_3]^+$ complex at 5.5 min (Figure 6). After 15 min at 100 °C (microwave), coordination of the $\{^{99m}Tc(CO)_3\}^+$ onto the silica particles was confirmed by radio-HPLC. In addition, gamma counting of the filtered reaction solution showed a decrease of activity in the solution to almost background level. Since **3** is randomly distributed over the surface of these model particles, the labeling with $^{99m}Tc$ is not preferential in the pores.
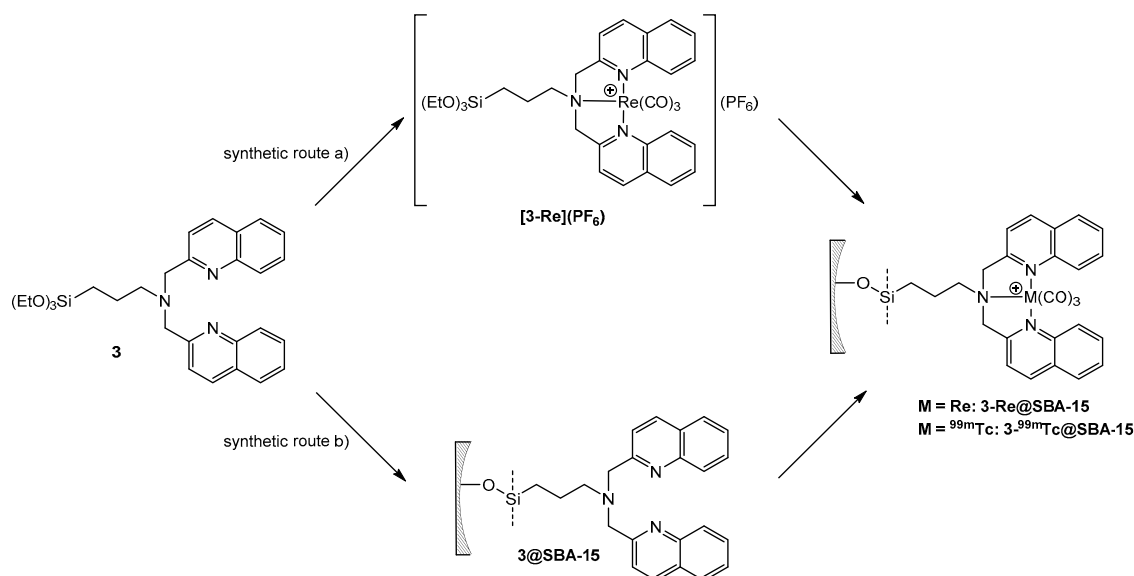


**Scheme 5.** Synthesis of silica particles "loaded" with Re via (a) grafting of **3-Re** or (b) solid phase supported synthesis. Synthetic route (b) corresponds to the labeling of the silica particles with $^{99m}Tc$.
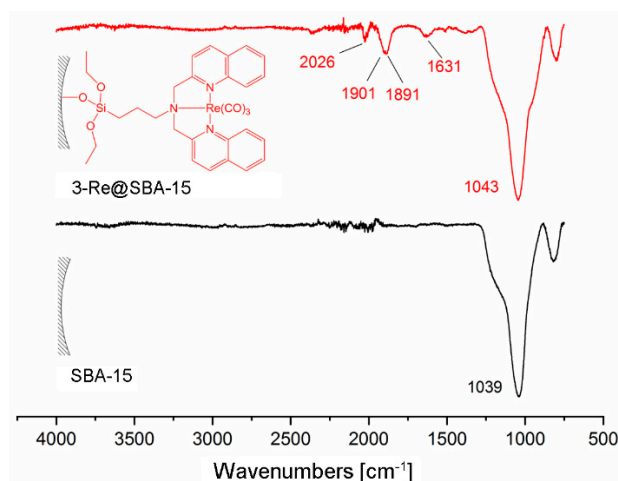


**Figure 5.** Comparison of the IR spectra of SBA-15 particles (black) and **3-Re@SBA-15** particles (red), synthesized by the reaction of $[Re(H_2O)_3(CO)_3]^+$ with **3-@SBA-15** (synthetic route b in Scheme 5). The CO vibrations at 2026, 1901, and 1891 cm$^{-1}$ show the coordination of the $\{Re(CO)_3\}^+$ moiety to **3**.

### 2.4. Synthesis and Labeling of a Bifunctional SBA-15 Construct with Re and $^{99m}Tc$

For the synthesis of a novel (nano)platform for theranostic applications, a bifunctionalized SBA-15 microparticle model construct was realized. In the synthesized model, a fluorescent dye, grafted preferentially to the external surface of the SBA-15 particles, mimics the targeting function. This was achieved with short reaction time, an apolar solvent (hexane), and a directing silane, such as 3-aminopropyltrimethoxyethoxyethoxysilane (APTMEES) [26]. Accordingly, the average pore size of the SBA-15 particles remained invariant upon the grafting of APTMEES (see Supplementary Materials)

in contrast to the grafting of **3** to unmodified SBA-15 particles. Subsequently, the grafted amino groups of APTMEES were reacted with the red emitting dye eosin isothiocyanate (EOITC). In the third step, **3** was grafted to the SBA-15 particles at the still accessible surface. Finally, the bifunctionalized **EOITC/3@SBA-15** particles were labeled with the $\{M(CO)_3\}^+$ (M = Re, $^{99m}$Tc) precursors (Scheme 6).
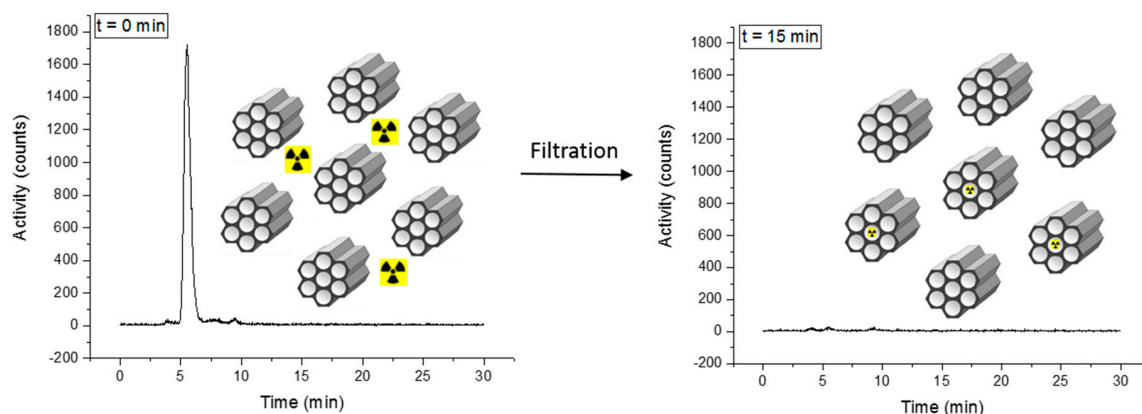


**Figure 6.** Idealized picture of the labeling of **3@SBA-15** with $[^{99m}Tc(H_2O)_3(CO)_3]^+$. Since **3** is randomly distributed over the surface of these model particles, the labeling with $^{99m}$Tc is not preferential in the pores. The radio-HPLC traces show the activity in the reaction solution. Left: The $\gamma$-signal of $[^{99m}Tc(H_2O)_3(CO)_3]^+$ is observed at 5.5 min (reaction time = 0). Right: almost quantitative coordination of $[^{99m}Tc(H_2O)_3(CO)_3]^+$ at the **3@SBA-15** particles (reaction time = 15 min) evidenced by disappearance of the 5.5 min peak.
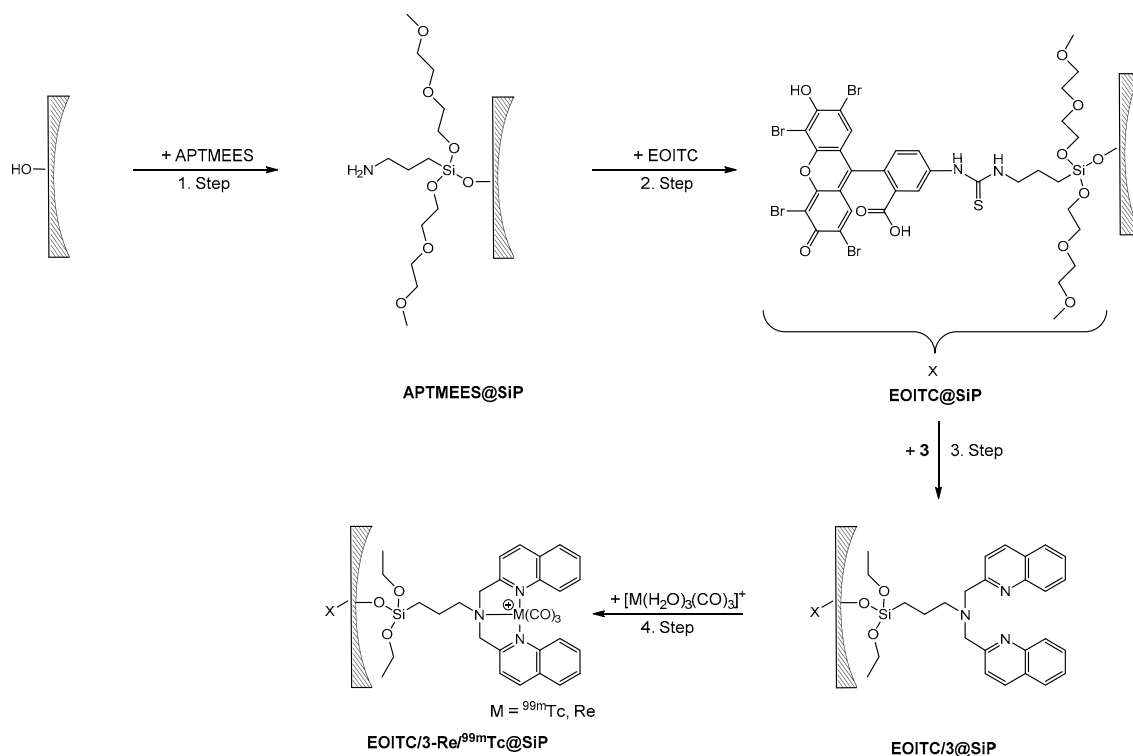


**Scheme 6.** Synthesis of bifunctionalized SBA-15 particles (SiP = SBA-15, spherical SBA-15 (sSBA-15)). Step 1: Grafting of APTMEES (10 min, room temperature). Step 2: Coupling of the fluorescent dye eosin isothiocyanate (EOITC) to the surface-grafted amino groups (16 h, room temperature). Step 3: Grafting of **3** (2 h, 40 °C). Step 4: Labeling of the **EOITC/3@SBA-15** particles with $\{M(CO)_3\}^+$ (M = Re, $^{99m}$Tc) precursors (pH 7; Re: 45 min, 100 °C; $^{99m}$Tc: 15 min, 100 °C).

Confocal laser scanning microscopy (CLSM) images of spherical SBA-15 (sSBA-15) prepared according to Scheme 6 show the location of the fluorescent moiety within the particles (Figure 7).
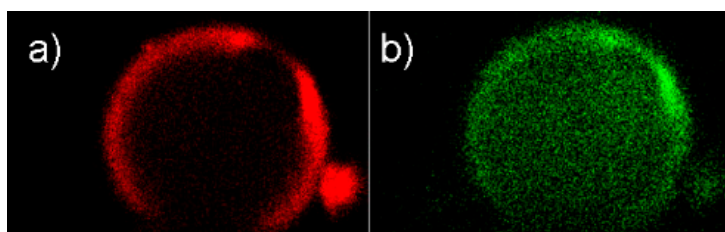


**Figure 7.** Selective bifunctionalization of sSBA-15 particles visualized by confocal laser scanning microscopy (CLSM): (**a**) red emission of the EOITC dye; (**b**) green emission of the **3-Re** complex.

By choosing different excitation wavelengths, the two moieties EOITC and **3-Re** can be excited separately in the same particle. Optical slices in the center of the particles were selected and representative images are shown in Figure 7. The red emission assessed the preferential attachment of EOITC on the external surface. The "loading" of the $\{Re(CO)_3\}^+$ complex to the pore surface is depicted by the green emission of the **3-Re** complex. Finally, the bifunctional **EOITC/3@sSBA-15** particles were labeled with $[^{99m}Tc(H_2O)_3(CO)_3]^+$ (Scheme 6, step 4). The reaction of $[^{99m}Tc(H_2O)_3(CO)_3]^+$ with **EOITC/3@sSBA-15** (5–15 MBq, pH 7, 15 min, 100 °C, microwave) led to labeling yields of 79%. Benchmarking this result, monofunctionalized particles that contained only **3** (**3@sSBA-15**) were reacted with $[^{99m}Tc(H_2O)_3(CO)_3]^+$ under the same labeling conditions, with a yield of 80%. The lower labeling yield of the **3@sSBA-15** particles (80%) vs. the **3@SBA-15** particles (>99%) described earlier in this report can be rationalized by the broader pore size distribution of the sSBA-15 particles. However, sSBA-15 particles had to be utilized to visualize the selective functionalization of the silica particles by CLSM. Further labeling studies of $[^{99m}Tc(H_2O)_3(CO)_3]^+$ with the precursor particles **APTMEES/3@sSBA** (Scheme 6, step 1), showed a labeling yield of only 68%. The decrease of 11% labeling yield (**APTMEES/3@sSBA** vs. **EOITC/3@sSBA-15)** has to be ascribed to electrostatic repulsion of the positively charged $[^{99m}Tc(H_2O)_3(CO)_3]^+$ molecules and the protonated amines of the APTMEES (saline solution, pH 7).

We show in this feasibility study synthetic pathways and procedures towards a SBA-15-based target-specific theranostic nanoplatform, utilizing the theranostic pair $^{99m}Tc/Re$. This platform enables the combination of optical (fluorescence) and radio imaging with radio- and chemotherapy. The translation into a theranostic nanoplatform can be realized as soon as procedures for the synthesis of well-defined, non-agglomerated SBA-15 nanoparticles have been established.

## 3. Materials and Methods

Caution: $^{99m}Tc$ is a γ-emitter. All experiments have to be performed in laboratories approved for working with low-level radioactive materials.

All chemicals were of reagent-grade quality or higher and were obtained from commercial suppliers. Solvents were used as received or dried over molecular sieves. $Na[^{99m}TcO_4]$ in 0.9% saline was eluted from a $^{99}Mo/^{99m}Tc$ Ultra-Technekow FM generator purchased from Mallinckrodt Medical B.V. (Petten, The Netherlands). $[^{99m}Tc(H_2O)_3(CO)_3]^+$ was synthesized according to an adapted version of a published procedure [58]. The $[^{99m}TcO_4]^-$ eluate (1–2 mL, obtained from the $^{99}Mo/^{99m}Tc$ generator) was added to a $N_2$-flushed microwave vial containing $Na_2(BH_3CO_2)$ (4 mg, 0.040 mmol), disodium tartrate dihydrate (7.0 mg, 0.030 mmol), and disodium tetraborate pentahydrate (7 mg, 0.024 mmol), and heated in a microwave reactor for 10 min at 110 °C. Finally, the pH of the solution was adjusted to pH 7 by the addition of 80–100 μL 1 M HCl. The $[^{99m}TcO_3(tacn)]^+$ was synthesized according a literature procedure [59].

Silica particles used in this study were of the MCM-41 and SBA-15 types. Due to their irregular morphological properties, such as size and shape, they are not suited for optical analysis by CLSM.

For that purpose, large spherical particles of the SBA-15 type (sSBA-15) were chosen. Besides these well-known microparticles of MCM-41 and SBA-15, hexagonal arrays of silica nanochannels (ASNCs), MCM-41-nanoparticles, and MCM-41 particles with various pore sizes were used in the initial screening. The particles were synthesized following literature procedures (sSBA-15 [26], ASNCSs [60], all others [61]). Characteristics of the applied silica particles are summarized in table S1 in the supplementary information.

High-resolution mass spectrometry (HR-ESI-MS) was performed on a Bruker maXis QTof high-resolution mass spectrometer (Bruker GmbH, Bremen, Germany).

$^1$H and $^{13}$C-NMR spectra were recorded in deuterated solvents on a Bruker AV-400 or Bruker AV-500 MHz spectrometer at 300 K. $^{13}$C-NMR spectra were proton decoupled. The chemical shifts ($\delta$) are reported in ppm relative to residual solvent peaks (dmf-d7 $^1$H: 8.03 ppm, $^{13}$C: 163.15 ppm; CDCl$_3$: $^1$H: 7.26 ppm, $^{13}$C: 77.16 ppm; MeOD: $^1$H: 3.31 ppm, $^{13}$C: 49.00 ppm; Acetone-d6: $^1$H: 2.05 ppm, $^{13}$C: 29.84 ppm). The abbreviations for the peak multiplicities are as follows: s (singlet), d (doublet), dd (doublet of doublets), t (triplet), q (quartet), m (multiplet), br (broad). $^{29}$Si-NMR spectra were recorded on a Bruker AV-500 MHz.

Gamma-counting of the $^{99m}$Tc solutions was performed on a COBRA 5002 (Packard Instrument, Meriden, USA). Half-life time corrections for the labeling of silica particles were neglected due to the sequential measurement of the samples, with less than 5 min between two samples. Labeling of silica particles: The initial activity of the $^{99m}$Tc-solutions was determined prior to the addition of the particle suspension. According to the dilution (factor 2), the activity for t = 0 min was calculated.

HPLC analyses were performed on a Merck Hitachi LaChrom L 7100 pump coupled to a Merck Hitachi LaChrom L7200 tunable UV detector (Hitachi, Tokyo, Japan) and a radiodetector. UV–Vis detection was performed at 250 nm. The detection of radioactive $^{99m}$Tc complexes was performed with a Berthold LB508 (Berthold Technologies, Bad Wildbad, Germany) radiodetector equipped with a bismuth germanium oxid (BGO) cell. Separations were achieved on a Macherey–Nagel C18 reversed-phase column (nucleosil 10 ml, 250/3 mm) using a gradient methanol (solvent A) and 0.1% trifluoroacetic acid (solvent B). Applied HPLC gradient: 0–3 min: 0% A, 100% B; 3–3.1 min: 0–25% A, 100–75% B; 3.1–9 min: 25% A, 75% B; 9–9.1 min: 25–34% A, 75–66% B; 9.1–18 min: 34–100% A, 66–0% B; 18–25 min: 100% A, 0% B; 25–25.1 min: 100–0% A, 0–100% B; 25.1–30 min: 0% A, 100% B. The flow rate was 0.5 mL·min$^{-1}$. Ultra performance liquid chromatography-electrospray ionization-mass spectrometry (UPLC-ESI-MS) was performed on a Waters Acquity UPLC System coupled to a Bruker high capacity ion trap mass spectrometer (HCTM), using an Acquity UPLC ethylene bridge hybrid (BEH) C18 1.7 μm (2.1 × 50 mm) column. UPLC solvents were formic acid (0.1% in millipore water) (solvent A) and acetonitrile HPLC grade (solvent B). Applied UPLC gradient: 0–0.5 min: 95% A, 5% B; 0.51–4.0 min: linear gradient from 95% A (5% B) to 0% A (100% B); 4–5 min: 100% B. The flow rate was 0.6 mL/min. Detection was performed at 250 nm and 480 nm (diode-array detector). For preparative HPLC, a Varian ProStar 320 system (Varian Inc, Palo Alto, USA) was used with a Dr. Maisch Reprosil C18 100-7 (40 × 250 mm) column. The solvents (HPLC grade) were 0.1% trifluoroacetic acid (solvent A) and acetonitrile (solvent B). Applied HPLC gradient: 0–2 min: 66% A (34% B); 2–45 min: linear gradient from 66% A (34% B) to 0% A (100% B); 45–51 min: 100% B. The flow rate was 40 mL/min. Detection was performed at 235 nm.

IR spectra were recorded on a Perkin-Elmer FT-IR Spectrum Two spectrometer (Perkin-Elmer Inc., Waltham, USA), using ATR technique and applied as neat samples.

Nitrogen sorption isotherms were collected at 77 K using a Quantachrome NOVA 3000 (Quantachrome Instruments, Boynton Beach, USA). Samples were vacuum-degassed at 80 °C for 3 h. The total specific surface area was calculated by the Brunauer-Emmett-Teller (BET) method [62]. Mesopore size distributions were evaluated by the nonlocal density functional theory (NLDFT) method [63] developed for silica exhibiting cylindrical pore geometry (NOVAWin software, Version 11.0, Quantachrome Instruments, Boynton Beach, USA). The adsorption branch of the respective isotherm was used for the calculations.

The fluorescence and CLSM setup consisted of an Olympus BX60 microscope equipped with a FluoView FV300 confocal unit and lasers operating at 488 and 543.5 nm.

UV–Vis spectra were measured on a Cary 50 UV–Vis spectrometer or a SPECORD® 250 PLUS spectrometer (Analytik Jena, Jena, Germany) with solution samples in 1 cm quartz cells.; $\lambda_{max}$ ($\varepsilon$) in nm; $\varepsilon$ in $M^{-1} \cdot cm^{-1}$. Fluorescence spectra were recorded with a LS 50 B Luminescence spectrometer (Perkin-Elmer Inc., Waltham, USA); $\lambda_{em}$ ($\lambda_{ex}$) in nm. Lifetime and transient absorption measurements were recorded on a LP920-K laser flash photolysis transient absorption spectrometer using a flash-lamp-pumped, Q-switched Nd:YAG laser (355 nm) as the excitation source. Probing of the sample was conducted by a Xe920 probe lamp (450 W) and an xP920 pulsing unit module. Argon-purged solution samples in 1 cm quartz cells were used.

Microwave reactions were performed with a Biotage Initiator+ Robot Eight (Biotage, Uppsala, Sweden) or Anton Paar Monowave 200 instrument (Anton Paar GmbH, Graz, Austria).

Automated C18 column flash chromatography was run on a Flash Master Solo with an Argonaut UV–Vis detector from Omnilab and a Gilson FC 204 fraction collector. Separations were achieved by using C18 silica gel from Supelco packed into an ISOLUTE reservoir (70 mL) from Biotage. Flash column solvents were bidistilled water (solvent A) and MeOH (solvent B). Applied flash column gradient: 0–10 min: 90% A, 10% B; 10–70 min: linear gradient from 90% A, 10% B to 0% A, 100% B; 70–90 min: 0% A, 100% B. The flow rate was 2.0 mL·min$^{-1}$. Detection was performed at 220 to 240 nm. ICP-MS measurements were performed on an Agilent QQQ 8800 Triple quad spectrometer (Agilent Technologies, Santa Carla, USA), equipped with standard x-lens settings, nickel cones, and a "micro-mist" quartz nebulizer. All solutions were prepared from 60% $HNO_3$ (Merck 1.1518.500 ultrapure) and 18.2 MΩ Millipore water (Merck KGaA, Darmstadt, Germany). Re (Merck 1.70344.0100 $H_2O$) was measured against a series of dilutions of single element standards (0–250 ng/mL).

Crystallographic data were collected at 183(2) K on a Rigaku OD XtaLAB Synergy Dualflex diffractometer (Rigaku Europe SE, Neu-Isenburg, Germany) equipped with a Pilatus 200 K detector and a PhotonJet Cu K$\alpha$ source ($\lambda = 1.54184$ Å) or Mo K$\alpha$ source ($\lambda = 0.71073$ Å). Suitable crystals were covered with oil (Infineum V8512, formerly known as Paratone N), placed on a nylon loop that was mounted in CrystalCap Magnetic™ (Hampton Research), and immediately transferred to the diffractometer. The program suite CrysAlis$^{Pro}$ was used for data collection, multi-scan absorption correction, and data reduction [64]. The structures were solved with direct methods using *SHELXS*-97 [65] and were refined by full-matrix least squares methods on $F^2$ with *SHELXL*-2014 [66]. The GUI ShelXle was employed [67].

For NMR, ICP-MS, and (HR)-ESI-MS measurements of functionalized silica particles, a precise amount of these particles (typically 5–10 mg) were decomposed at room temperature for 1–20 h in 1 M NaOD in $D_2O$ (typically 0.7 mL) for NMR or 1M NaOH (typically 0.7 mL) for MS.

Detailed synthetic procedures for all reported reactions as well as control reactions are described in the supplementary information.

### 3.1. Synthesis of **1d**

The 2-quinolinecarboxaldehyde (825 mg, 5.25 mmol) was dissolved in 1,2-dichloroethane (28 mL) and 4-aminobutyric acid (258 mg, 2.50 mmol) was added and stirred for 2 h at room temperature. Sodium triacetoxyborohydride (1.219 g, 5.75 mmol) was added and the solution was stirred at r.t. for 3 h. The 1,2-dichloroethane was evaporated in vacuo, the crude product was redissolved in dichloromethane (25 mL), and washed with $H_2O$ (3 × 25 mL). The organic phase was dried in vacuo and purified by flash chromatography over C-18 silica, resulting in **1d** (277 mg, 0.719 mmol, 29%).

HR-MS (ESI): calcd. for $[C_{24}H_{23}N_3O_2+H]^+$: 386.18630, found: 386.18664. $^1$H-NMR (400 MHz, CDCl$_3$) δ = 8.08–8.06 (m, 4H), 7.73 (d, *J* = 8.1 Hz, 2H), 7.68–7.61 (m, 4H), 7.48 (t, *J* = 7.5 Hz, 2H), 4.05 (s, 4H), 2.75 (t, *J* = 6.1 Hz, 2H), 2.37 (t, *J* = 6.6 Hz, 2H), 1.95–1.89 (m, 2H). $^{13}$C NMR (126 MHz, CDCl$_3$) δ = 177.13, 159.22, 147.41, 136.98, 129.78, 128.75, 127.67, 127.49, 126.53, 121.53, 60.84, 54.82, 34.20, 22.54.

IR: 3061w, 2946w, 2814w, 1957w, 1701m, 1620w, 1598m, 1564w, 1504m, 1428m, 1308w, 1240m, 1112m, 907w, 826s, 732s.

### 3.2. Synthesis of 2

The **1d** (28 mg, 0.07 mmol), 3-aminopropyltriethoxysilane (17.7 mg, 18.7 μL, 0.08 mmol) and hexafluorophosphate benzotriazole tetramethyl uronium (82.6 mg, 0.22 mmol) were dissolved in dry DMF (3 mL) and *N,N*-diisopropylethylamine (28 mg, 37.24 μL, 0.22 mmol) was added. The mixture was stirred at r.t. for 2 h. The organic phase was washed with $H_2O$ (3 × 10 mL), filtered, and the DMF was evaporated under reduced pressure to yield **2** (35 mg, 0.06 mmol, 85%).

HR-MS (ESI:) calcd. for $[C_{33}H_{45}N_4O_4Si+H]^+$: 589.32119, found: 589.32046. ^{1}H-NMR (400 MHz, $CDCl_3$) δ = 8.08 (d, *J* = 8.5 Hz, 2H), 8.04 (d, *J* = 8.4 Hz, 2H), 7.77 (d, *J* = 8.1 Hz, 2H), 7.68 (t, *J* = 7.6 Hz, 2H), 7.63 (d, *J* = 8.4 Hz, 2H), 7.50 (t, *J* = 7.5 Hz, 2H), 4.01 (s, 4H), 3.77 (q, *J* = 7.0 Hz, 6H), 3.10 (q, *J* = 6.6 Hz, 2H), 2.68 (t, *J* = 6.8 Hz, 2H), 2.17 (t, *J* = 7.4 Hz, 2H), 1.95–1.88 (m, 2H), 1.56–1.48 (m, 2H), 1.19 (t, *J* = 7.0 Hz, 9H), 0.56–0.52 (m, 2H). ^{13}C NMR (126 MHz, $CDCl_3$) δ = 172.88, 160.55, 147.69, 136.40, 129.56, 129.12, 127.65, 127.45, 126.31, 121.41, 61.52, 58.56, 54.35, 41.97, 34.66, 23.81, 23.06, 18.42, 7.90.

### 3.3. Synthesis of 3

The 2-quinolinecarboxaldehyde (128 mg, 0.81 mmol) was dissolved in 1,2-dichloroethane (20 mL) and 3-aminopropyltriethoxysilane (87 mg, 92 μL, 0.40 mmol) was added. The mixture was stirred at 25 °C for 2 h, sodium triacetoxyborohydride (252 mg, 1.18 mmol) was added, and the mixture was stirred for 3.5 h at 25 °C. The 1,2-dichloroethane was evaporated in vacuo, EtOH (15 mL) was added, and stirred for 10 min at 25 °C. The EtOH was evaporated in vacuo. The residue was washed with toluene (20 mL) and the yellow solution was separated from the white precipitate by centrifugation. The toluene was evaporated to yield crude **3**. The product was purified by flash chromatography over C-18 silica, leading to the isolation of **3** (99 mg, 0.197 mmol, 49%).

HR-MS (ESI:) calcd. for $[C_{29}H_{37}N_3O_3Si+H]^+$: 504.26770, found: 504.26794. ^{1}H-NMR (400 MHz, $CDCl_3$) δ = 8.11 (d, *J* = 8.5 Hz, 2H), 8.04 (d, *J* = 8.5 Hz, 2H), 7.78-7.74 (m, 4H), 7.67 (t, *J* = 7.6 Hz, 2H), 7.49 (t, *J* = 7.4 Hz, 2H), 4.02 (s, 4H), 3.72 (q, *J* = 7.0 Hz, 4H), 2.63 (t, *J* = 7.3 Hz, 2H), 1.72–1.64 (m, 2H), 1.14 (t, *J* = 7.0 Hz, 9H), 0.58–0.54 (m, 2H). ^{13}C-NMR (126 MHz, $CDCl_3$) δ = 161.0, 147.7, 136.4, 129.5, 129.2, 127.6, 127.5, 126.2, 121.2, 61.7, 58.5, 58.0, 20.8, 18.4, 8.1. ^{29}Si-NMR (99.36 MHz, $CDCl_3$): δ = −45.01 ppm. IR: 2975w, 2928w, 2881w, 1600m, 1506m, 1429w, 1390w, 1313w, 1164w, 1100s, 1074s, 950m, 831m, 767s.

### 3.4. General Procedure for the Synthesis of {Re(CO)₃}⁺ Complexes

Between 0.15 and 0.01 mmol of the ligands (**1a**, **1b**, **1e**, and **3**) were dissolved in 1 to 5 mL MeOH ($[(3)Re(CO)_3]^+$ = EtOH) and equimolar amounts of $(NEt_4)_2[ReBr_3(CO)_3]$ were added. A microwave vial containing the reaction solution was purged with $N_2$ for 5 min. The mixture was heated to 85 °C (110 °C for $[(1e)Re(CO)_3]^+$ and $[(3)Re(CO)_3]^+$) for 45 min in a microwave reactor. $H_2O$ was added to the vial and the formed precipitate was removed by filtration or centrifugation. From the clear solution, the product was precipitated by the addition of $NH_4PF_6$ as the corresponding $PF_6$ salt and collected by filtration or centrifugation. The $[(3)Re(CO)_3](PF_6)$ was directly precipitated from the aqueous solution by the addition of $NH_4PF_6$. The products were washed with several mL of $H_2O$ and dried under high vacuum.

### 3.4.1. Analytical Data for [(**1a**)Re(CO)₃](PF₆)

HR-MS (ESI:) calcd. for $[C_{26}H_{21}N_3O_3Re]^+$: 610.11349, found: 610.11355. ^{1}H-NMR (500 MHz, $CDCl_3$) δ = 8.48 (d, *J* = 8.8 Hz, 2H), 8.36 (d, *J* = 8.4 Hz, 2H), 7.90 (d, *J* = 8.0 Hz, 2H), 7.84 (t, *J* = 7.5 Hz, 2H), 7.66 (m, 4H), 6.31 (m, 1H), 5.77 (d, *J* = 16.8 Hz, 1H), 5.69 (d, *J* = 10.2 Hz, 1H), 5.08 (m, 4H), 4.32 (d, *J* = 7.1 Hz, 2H). ^{13}C-NMR (125 MHz, $CDCl_3$) δ = 195.62, 194.14, 164.48, 147.11, 141.89, 133.24, 129.82, 129.59, 128.58, 128.54, 128.43, 127.34, 120.17, 70.42, 68.85. IR: 2026s (CO), 1903s (CO), 1712w, 1604w, 1516w, 1432w, 1369w, 1291w, 1217w, 1149w, 1124w, 948w, 835s 747w.

Crystals suitable for X-ray diffraction analysis were obtained by vapor diffusion of cyclohexane into a THF solution of [(**1a**)Re(CO)$_3$](PF$_6$).

### 3.4.2. Analytical Data for [(**1b**)Re(CO)$_3$](PF$_6$)

HR-MS (ESI:) calcd. for [C$_{29}$H$_{27}$N$_3$O$_5$Re]$^+$: 684.15027, found: 684.14980. $^1$H-NMR (400 MHz, CDCl$_3$) δ = 8.49 (d, *J* = 8.7 Hz, 2H), 8.34 (d, *J* = 8.4 Hz, 2H), 7.91 (dd, *J* = 3.1 Hz, 2H), 7.85–7.81 (m, 2H), 7.66 (t, *J* = 7.2 Hz, 2H), 7.60 (d, *J* = 8.4 Hz, 2H), 5.25–5.13 (m, 4H), 4.48 (s, 2H), 1.45 (s, 9H). $^{13}$C-NMR (125 MHz, CDCl$_3$) δ = 195.54, 193.76, 166.65, 164.76, 147.02, 141.62, 133.15, 129.81, 128.59, 128.52, 128.30, 119.74, 84.83, 70.40, 66.83, 28.09. IR: 2159w, 2027s (CO), 1910s (CO), 1735w, 1519w, 1370w, 1243w, 1160m, 1034w, 844s, 780w.

Crystals suitable for X-ray diffraction analysis were obtained by vapor diffusion of cyclohexane into a THF solution of [(**1b**)Re(CO)$_3$](PF$_6$).

### 3.4.3. Analytical Data for [(**1e**)Re(CO)$_3$](PF$_6$)

HR-MS (ESI:) calcd. for [C$_{26}$H$_{22}$N$_3$O$_4$Re]$^+$: 628.12406, found: 628.12394. $^1$H-NMR (400 MHz, CDCl$_3$) δ = 8.47 (d, *J* = 3.1 Hz, 2H), 8.35 (d, *J* = 8.3 Hz, 2H), 7.89 (d, *J* = 3.2 Hz, 2H), 7.85–7.81 (m, 2H), 7.68–7.63 (m, 4H), 5.16–5.04 (m, 4H), 3.99–3.95 (m, 2H), 3.84 (t, *J* = 5.6 Hz, 2H), 2.30–2.23 (m, 2H). $^{13}$C-NMR (126 MHz, CDCl$_3$) δ = 195.72, 194.15, 164.64, 147.10, 141.87, 133.21, 129.78, 128.59, 128.55, 128.43, 120.21, 68.70, 65.93, 59.80, 29.23. IR: 3617w, 2919w, 2025s (CO), 1932m (CO), 1897s (CO) 1597w, 1519w, 1435w, 1371w, 1306w, 1214w, 1126w, 1047w, 831s, 742m, 659m.

Crystals suitable for X-ray diffraction analysis were obtained by vapor diffusion of cyclohexane into a THF solution of [(**1e**)Re(CO)$_3$](PF$_6$).

### 3.4.4. Analytical Data for [**3-Re**](PF$_6$)

HR-MS (ESI:) calcd. for [C$_{32}$H$_{37}$N$_3$O$_6$ReSi]$^+$: 774.20036, found: 774.20035. $^1$H-NMR (500 MHz, CDCl$_3$) δ = 8.46 (d, *J* = 8.8 Hz, 2H), 8.33 (d, *J* = 8.5 Hz, 2H), 7.88 (d, *J* = 8.0 Hz, 2H), 7.83–7.80 (m, 2H), 7.66–7.63 (m, 4H), 5.19–4.96 (m, 4H), 3.84 (q, *J* = 7.0 Hz, 6H), 2.16–2.10 (m, 2H), 1.58 (s, 2H), 1.20 (t, *J* = 7.0 Hz, 9H), 0.75 (t, *J* = 7.7 Hz, 2H). $^{13}$C-NMR (126 MHz, CDCl$_3$) δ = 195.8, 194.2, 164.7, 147.1, 141.8, 133.1, 129.8, 128.6, 128.5, 128.4, 120.3, 70.7, 68.7, 58.8, 20.4, 18.4, 7.7. $^{29}$Si-NMR (99.38 MHz, CDCl$_3$): δ = −47.44 ppm. IR: 2976w, 2891w, 2025s (CO), 1901s (CO), 1602w, 1517w, 1470w, 1436w, 1394w, 1300w, 1205w, 1163w, 1074m, 958w, 873w, 835s, 779m, 749m, 647w. UV–Vis (CHCl$_3$, 10$^{-5}$ M): 323 nm (13696 M$^{-1}$·cm$^{-1}$). Fluorescence (CHCl$_3$, 10$^{-5}$ M): λ$_{ex}$ (326), λ$_{em}$ air (426, 546), λ$_{em}$ N$_2$ (383, 566).

### 3.5. Synthesis of *3@SBA-15*

SBA-15 particles (213 mg) were dried by heating (140 °C) under high vacuum for 4 h. Then, **3** (10 mg, 0.02 mmol) was dissolved in dry toluene (5 mL) and added to the SBA-15 particles. The suspension was sonicated at 60 °C for 2 h. Filtration, washing with toluene (5 mL) and Et$_2$O (5 mL), and drying under high vacuum led to the isolation of **3@SBA-15** (176 mg).

EA: C 2.46, H 0.49, N 0.32. HR-ESI of dissolved particles (1M NaOD in D$_2$O): calc. for [C$_{23}$H$_{25}$O$_3$N$_3$Si+H]$^+$: 420.17379, found: 420.17345. $^1$H-NMR (1M NaOD in D$_2$O 500 MHz): δ = 7.76 (d, *J* = 8.5 Hz, 2H), 7.56 (d, *J* = 8.3 Hz, 2H), 7.52–7.49 (m, 4H), 7.34 (t, *J* = 7.0 Hz, 2H), 7.24 (d, *J* = 8.5 Hz, 2H), 3.88 (s, 4H), 2.70 (t, *J* = 7.8 Hz, 2H), 1.72–1.69 (m, 2H), 0.38 (t, *J* = 8.4 Hz, 2H).

### 3.6. Synthesis of *3-Re@SBA-15*

#### 3.6.1. Method A: Grafting of **3-Re** onto **SBA15**

SBA-15 particles were dried by heating (140 °C) under high vacuum for 4 h. The dry SBA-15 particles (200 mg) were dispersed in dry DCM (5 mL). The suspension was transferred into a microwave vial and [**3-Re**](PF$_6$) (9.2 mg, 0.01 mmol) was added. The suspension was sonicated for 2 h at 60 °C.

After filtration, washing with DCM (3 mL), and drying under high vacuum, **3-Re@SBA-15** (202 mg) was isolated.

EA: Found: C 2.70, H 0.57, N 0.21. IR: 2026w (CO), 1901w (CO), 1891w (CO), 1631w, 1053s (Si–O), 964m, 818w, 649w.

### 3.6.2. Method B: Reaction of $(NEt_4)_2[Re(H_2O)_3(CO)_3]$ with **3@SBA-15**

$(NEt_4)_2[Re(CO)_3Br_3]$ (38.4 mg, 0.050 mmol) was dissolved in $H_2O$ (6 mL) and $AgNO_3$ (25.2 mg, 0.148 mmol) was added. The solution turned milky and a precipitate was formed immediately. After stirring for 60 min at r.t. the precipitate was filtered. A clear solution $[Re(H_2O)_3(CO)_3]NO_3$ was obtained (pH 6–7). This solution was added to **3@SBA-15** (80 mg) particles and the suspension was heated at 100 °C for 45 min in a microwave reactor. Finally, **3-Re@SBA-15** (71 mg) was isolated by filtration, washed with $H_2O$ (2 mL) and toluene (4 mL), and dried under vacuum.

EA: C: 2.28 H: 0.80 N: 0.30. Nitrogen sorption: BET: 217 $m^2$/g; average pore size: 7.0 nm; total pore volume: 0.43 $cm^3$/g. IR: 2026w (CO), 1901w (CO), 1891w (CO), 1631w, 1053s (Si–O), 964 m, 818w, 649w. ICP-MS: 1.4% w; 0.077 mmol/g particles; 0.07 Re atoms/$nm^2$.

### 3.7. Synthesis of Bifunctionalized Mesoporous Silica Particles (**EOITC/3@SiP**)

Silica particles (SiP = SBA-15, spherical sSBA-15) were dried by heating (140 °C) under high vacuum for 4 h, then dispersed in hexane, and 3-aminopropyltris(methoxyethoxyethoxy)silane (APTMEES) was added. The suspension was sonicated for 10 min at room temperature. The particles were recovered by filtration, washed with hexane (3 × 3 mL), and dried under high vacuum, yielding **APTMEES@SiP**. Eosin isothiocyanate (EOITC) was dissolved in EtOH (10 mL). **APTMEES@SiP** particles were added and the suspension was stirred at r.t. for 16 h. The particles were collected by filtration, washed with EtOH (50 mL) and $H_2O$ (50 mL), yielding **EOITC/@SiP**. Then, **3** was dissolved in dry toluene and added to dry **EOITC/@SiP** particles. The suspension was sonicated at 40 °C for 2 h. Finally, **EOITC/3@SiP** was filtered off, washed with toluene (5 mL) and $Et_2O$ (5 mL), and dried under high vacuum.

### 3.8. Reaction of Bifunctionalized Mesoporous Silica Particles (**SiP**) with $[Re(H_2O)_3(CO)_3]^+$

The $(NEt_4)_2[Re(CO)_3Br_3]$ was dissolved in $H_2O$ and 3 equiv $AgNO_3$ were added. A colorless precipitate was formed immediately. After stirring for 60 min at r.t. the precipitate was filtered off. A clear solution of $[Re(H_2O)_3(CO)_3]NO_3$ was obtained (pH 6–7). This solution was added to the **EOITC/3@SiP** (SiP = SBA-15, spherical sSBA-15) and the suspension was heated at 100 °C for 45 min by means of a microwave reactor. The formed **EOITC/3-Re@SiP** particles were collected by filtration, washed with $H_2O$ (2 mL) and toluene (4 mL), and dried under vacuum.

### 3.9. Labeling of Bifunctionalized Mesoporous Silica Particles (**SiP**) with $[^{99m}Tc(H_2O)_3(CO)_3]^+$

A microwave vial was charged with **EOITC/3@SiP** (SiP = SBA-15, sSBA-15) (10 mg) and saline (2 mL). The vial was flushed with $N_2$ (5 min). The $[^{99m}Tc(H_2O)_3(CO)_3]^+$ (5–15 MBq) in saline (2 mL, pH 7) was added and the suspension was heated at 100 °C for 15 min in the microwave reactor. For reaction control, an aliquot (0.5 mL) was filtered and centrifuged, and the clear solution was used for radio-HPLC measurements. As an additional control, 10 µL of each centrifuged sample was collected and the remaining activity in solution was determined by means of a γ-counter.

## 4. Conclusions

We combined the multimodal properties of the bisquinoline/{M(CO)$_3$}$^+$ system (M = $^{99m}$Tc, Re) with the theranostic properties of the $^{99m}$Tc/$^{186/188}$Re pair at a mesoporous silica support. The presented synthetic procedures are based on fundamental studies, which disclosed the most suitable mesoporous silica construct (SBA-15) for this development. Furthermore, a variety of different pathways was developed to synthesize bisquinoline-containing silanes, suitable for grafting reactions with silica

particles. The hydrolysis of the trialkoxysilane moiety and subsequent cross-linking of the products had to be addressed. The successful functionalization of the external and the pore surface of the mesoporous silica particles was visualized by confocal laser scanning microscopy. The synthesized model system mimics a SBA-15-based target-specific theranostic nanoplatform, which enables the combination of fluorescence and radio imaging with the possibility of radio- and chemotherapy. Currently, we are using the reported procedures to synthesize target-specific nanoparticles for the first in vitro and in vivo studies.

## References

1. Arano, Y. Recent advances in $^{99m}$Tc radiopharmaceuticals. *Ann. Nucl. Med.* **2002**, *16*, 79–93. [CrossRef] [PubMed]

2. Arano, Y. Recent advances in $^{99m}$Tc radiopharmacenticals. *J. Nucl. Radiochem. Sci.* **2005**, *6*, 177–181. [CrossRef]

3. Bartholomä, M.D.; Louie, A.S.; Valliant, J.F.; Zubieta, J. Technetium and gallium derived radiopharmaceuticals: Comparing and contrasting the chemistry of two important radiometals for the molecular imaging era. *Chem. Rev.* **2010**, *110*, 2903–2920. [CrossRef] [PubMed]

4. Liu, S.; Chakraborty, S. $^{99m}$Tc-centered one-pot synthesis for preparation of $^{99m}$Tc radiotracers. *Dalton Trans.* **2011**, *40*, 6077–6086. [CrossRef]

5. Papagiannopoulou, D. Technetium-99m radiochemistry for pharmaceutical applications. *J. Label. Compd. Radiopharm.* **2017**, *60*, 502–520. [CrossRef]

6. Lepareur, N.; Lacœuille, F.; Bouvry, C.; Hindré, F.; Garcion, E.; Chérel, M.; Noiret, N.; Garin, E.; Knapp, F.F.R. Rhenium-188 labeled radiopharmaceuticals: Current clinical applications in oncology and promising perspectives. *Front. Med.* **2019**, *6*, 132. [CrossRef]

7. Meola, G.; Braband, H.; Jordi, S.; Fox, T.; Blacque, O.; Spingler, B.; Alberto, R. Structure and reactivities of rhenium and technetium bis-arene sandwich complexes [M($\eta^6$-arene)$_2$]$^+$. *Dalton Trans.* **2017**, *46*, 14631–14637. [CrossRef]

8. Stephenson, K.A.; Banerjee, S.R.; Besanger, T.; Sogbein, O.O.; Levadala, M.K.; McFarlane, N.; Lemon, J.A.; Boreham, D.R.; Maresca, K.P.; Brennan, J.D.; et al. Bridging the Gap between In Vitro and In Vivo imaging: Isostructural Re and ^{99m}Tc complexes for correlating fluorescence and radioimaging studies. *J. Am. Chem. Soc.* **2004**, *126*, 8598–8599. [CrossRef]

9. Agrawal, U.; Gupta, M.; Jadon, R.S.; Sharma, R.; Vyas, S.P. Multifunctional nanomedicines: Potentials and prospects. *Drug Deliv. Transl. Res.* **2013**, *3*, 479–497. [CrossRef]

10. Longmire, M.R.; Ogawa, M.; Choyke, P.L.; Kobayashi, H. Biologically optimized nanosized molecules and particles: More than just size. *Bioconjugate Chem.* **2011**, *22*, 993–1000. [CrossRef]

11. He, J.; Liu, G.; Gupta, S.; Zhang, Y.; Rusckowski, M.; Hnatowich, D.J. Amplification targeting: A modified pretargeting approach with potential for signal amplification—Proof of a concept. *J. Nucl. Med.* **2004**, *45*, 1087–1095. [PubMed]

12. Rousseau, V.; Denizot, B.; Pouliquen, D.; Jallet, P.; Le Jeune, J.J. Investigation of blood-brain barrier permeability to magnetite-dextran nanoparticles (MD3) after osmotic disruption in rats. *Magn. Reson. Mater. Phys. Biol. Med.* **1997**, *5*, 213–222. [CrossRef] [PubMed]

13. Chao-Ming, F.; Yuh-Feng, W.; Yu-Chiang, C.; Shih-Hung, H.; Ming-Da, Y. Directly labeling ferrite nanoparticles with Tc-99m radioisotope for diagnostic applications. *IEEE Trans. Magn.* **2004**, *40*, 3003–3005. [CrossRef]

14. Chao-Ming, F.; Yuh-Feng, W.; Yu-Feng, G.; Tang-Yi, L.; Jainn-Shiun, C. In Vivo bio-distribution of intravenously injected Tc-99m labeled ferrite nanoparticles bounded with biocompatible medicals. *IEEE Trans. Magn.* **2005**, *41*, 4120–4122. [CrossRef]

15. Chan, H.B.S.; Ellis, B.L.; Sharma, H.L.; Frost, W.; Caps, V.; Shields, R.A.; Tsang, S.C. Carbon-encapsulated radioactive ^{99m}Tc nanoparticles. *Adv. Mater.* **2004**, *16*, 144–149. [CrossRef]

16. Park, S.H.; Gwon, H.J.; Shin, J. Synthesis of ^{99m}Tc-labeled organo-germanium nanoparticles and their in vivo study as a spleen imaging agent. *J. Label. Compd. Radiopharm.* **2006**, *49*, 1163–1170. [CrossRef]

17. Guo, J.; Zhang, X.; Li, Q.; Li, W. Biodistribution of functionalized multiwall carbon nanotubes in mice. *Nucl. Med. Biol.* **2007**, *34*, 579–583. [CrossRef]

18. Xu, J.-Y.; Li, Q.-N.; Li, J.-G.; Ran, T.-C.; Wu, S.-W.; Song, W.-M.; Chen, S.-L.; Li, W.-X. Biodistribution of [99m]Tc-$C_{60}(OH)_x$ in Sprague–Dawley rats after intratracheal instillation. *Carbon* **2007**, *45*, 1865–1870. [CrossRef]

19. Douglas, S.J.; Davis, S.S.; Illum, L. Biodistribution of poly(butyl 2-cyanoacrylate) nanoparticles in rabbits. *Int. J. Pharm.* **1986**, *34*, 145–152. [CrossRef]

20. Park, K.-H.; Song, H.-C.; Na, K.; Bom, H.-S.; Lee, K.H.; Kim, S.; Kang, D.; Lee, D.H. Ionic strength-sensitive pullulan acetate nanoparticles (PAN) for intratumoral administration of radioisotope: Ionic strength-dependent aggregation behavior and [99m]Technetium retention property. *Colloids Surf. B* **2007**, *59*, 16–23. [CrossRef]

21. Banerjee, T.; Mitra, S.; Kumar Singh, A.; Kumar Sharma, R.; Maitra, A. Preparation, characterization and biodistribution of ultrafine chitosan nanoparticles. *Int. J. Pharm.* **2002**, *243*, 93–105. [CrossRef]

22. Banerjee, T.; Singh, A.K.; Sharma, R.K.; Maitra, A.N. Labeling efficiency and biodistribution of Technetium-99m labeled nanoparticles: Interference by colloidal tin oxide particles. *Int. J. Pharm.* **2005**, *289*, 189–195. [CrossRef] [PubMed]

23. Reddy, L.H.; Sharma, R.K.; Chuttani, K.; Mishra, A.K.; Murthy, R.R. Etoposide-incorporated tripalmitin nanoparticles with different surface charge: Formulation, characterization, radiolabeling, and biodistribution studies. *AAPS J.* **2004**, *6*, 23. [CrossRef] [PubMed]

24. Fischer, H.C.; Chan, W.C.W. Nanotoxicity: The growing need for in vivo study. *Curr. Opin. Biotechnol.* **2007**, *18*, 565–571. [CrossRef] [PubMed]

25. Wu, S.-H.; Hung, Y.; Mou, C.-Y. Mesoporous silica nanoparticles as nanocarriers. *Chem. Commun.* **2011**, *47*, 9972–9985. [CrossRef] [PubMed]

26. Gartmann, N.; Brühwiler, D. Controlling and imaging the functional-group distribution on mesoporous silica. *Angew. Chem. Int. Ed.* **2009**, *48*, 6354–6356. [CrossRef]

27. Ramm, J.H.; Gartmann, N.; Brühwiler, D. Direct synthesis and fluorescent imaging of bifunctionalized mesoporous iodopropyl-silica. *J. Colloid Interface Sci.* **2010**, *345*, 200–205. [CrossRef]

28. Schlipf, D.M.; Rankin, S.E.; Knutson, B.L. Selective external surface functionalization of large-pore silica materials capable of protein loading. *Microporous Mesoporous Mat.* **2017**, *244*, 199–207. [CrossRef]

29. Zucchetto, N.; Brühwiler, D. Strategies for localizing multiple functional groups in mesoporous silica particles through a one-pot synthesis. *Chem. Mater.* **2018**, *30*, 7280–7286. [CrossRef]

30. Sharma, K.K.; Anan, A.; Buckley, R.P.; Ouellette, W.; Asefa, T. Toward efficient nanoporous catalysts: Controlling site-isolation and concentration of grafted catalytic sites on nanoporous materials with solvents and colorimetric elucidation of their site-isolation. *J. Am. Chem. Soc.* **2008**, *130*, 218–228. [CrossRef]

31. Sharma, K.K.; Asefa, T. Efficient bifunctional nanocatalysts by simple postgrafting of spatially isolated catalytic groups on mesoporous materials. *Angew. Chem. Int. Ed.* **2007**, *46*, 2879–2882. [CrossRef] [PubMed]

32. Wang, X.; Lin, K.S.K.; Chan, J.C.C.; Cheng, S. Direct synthesis and catalytic applications of ordered large pore aminopropyl-functionalized SBA-15 mesoporous materials. *J. Phys. Chem. B* **2005**, *109*, 1763–1769. [CrossRef] [PubMed]

33. Brunel, D. Functionalized micelle-templated silicas (MTS) and their use as catalysts for fine chemicals. *Microporous Mesoporous Mat.* **1999**, *27*, 329–344. [CrossRef]

34. Macquarrie, D.J.; Jackson, D.B. Aminopropylated MCMs as base catalysts: A comparison with aminopropylated silica. *Chem. Commun.* **1997**, *18*, 1781–1782. [CrossRef]

35. Cauvel, A.; Renard, G.; Brunel, D. Monoglyceride synthesis by heterogeneous catalysis using MCM-41 type silicas functionalized with amino groups. *J. Org. Chem.* **1997**, *62*, 749–751. [CrossRef] [PubMed]

36. Liu, A.M.; Hidajat, K.; Kawi, S.; Zhao, D.Y. A new class of hybrid mesoporous materials with functionalized organic monolayers for selective adsorption of heavy metal ions. *Chem. Commun.* **2000**, 1145–1146. [CrossRef]

37. Vallet-Regí, M.; Balas, F.; Arcos, D. Mesoporous materials for drug delivery. *Angew. Chem. Int. Ed.* **2007**, *46*, 7548–7558. [CrossRef]

38. Angelos, S.; Johansson, E.; Stoddart, J.F.; Zink, J.I. Mesostructured silica supports for functional materials and molecular machines. *Adv. Funct. Mater.* **2007**, *17*, 2261–2271. [CrossRef]

39. Mal, N.K.; Fujiwara, M.; Tanaka, Y. Photocontrolled reversible release of guest molecules from coumarin-modified mesoporous silica. *Nature* **2003**, *421*, 350–353. [CrossRef]

40. Lai, C.-Y.; Trewyn, B.G.; Jeftinija, D.M.; Jeftinija, K.; Xu, S.; Jeftinija, S.; Lin, V.S.Y. A mesoporous silica nanosphere-based carrier system with chemically removable CdS nanoparticle caps for stimuli-responsive controlled release of neurotransmitters and drug molecules. *J. Am. Chem. Soc.* **2003**, *125*, 4451–4459. [CrossRef]

41. Muñoz, B.; Rámila, A.; Pérez-Pariente, J.; Díaz, I.; Vallet-Regí, M. MCM-41 organic modification as drug delivery rate regulator. *Chem. Mater.* **2002**, *15*, 500–503. [CrossRef]

42. Argyo, C.; Weiss, V.; Bräuchle, C.; Bein, T. Multifunctional mesoporous silica nanoparticles as a universal platform for drug delivery. *Chem. Mater.* **2014**, *26*, 435–451. [CrossRef]

43. Giret, S.; Wong Chi Man, M.; Carcel, C. Mesoporous-silica-functionalized nanoparticles for drug delivery. *Chem. Eur. J.* **2015**, *21*, 13850–13865. [CrossRef] [PubMed]

44. Riehemann, K.; Schneider, S.W.; Luger, T.A.; Godin, B.; Ferrari, M.; Fuchs, H. Nanomedicine—Challenge and perspectives. *Angew. Chem. Int. Ed.* **2009**, *48*, 872–897. [CrossRef] [PubMed]

45. Beck, J.S.; Vartuli, J.C.; Roth, W.J.; Leonowicz, M.E.; Kresge, C.T.; Schmitt, K.D.; Chu, C.T.W.; Olson, D.H.; Sheppard, E.W.; McCullen, S.B.; et al. A new family of mesoporous molecular sieves prepared with liquid crystal templates. *J. Am. Chem. Soc.* **1992**, *114*, 10834–10843. [CrossRef]

46. Kievsky, Y.; Sokolov, I. Self-assembly of uniform nanoporous silica fibers. *IEEE TNANO* **2005**, *4*, 490–494. [CrossRef]

47. Zhao, D.; Huo, Q.; Feng, J.; Chmelka, B.F.; Stucky, G.D. Nonionic triblock and star diblock copolymer and oligomeric surfactant syntheses of highly ordered, hydrothermally stable, mesoporous silica structures. *J. Am. Chem. Soc.* **1998**, *120*, 6024–6036. [CrossRef]

48. Braband, H.; Tooyama, Y.; Fox, T.; Alberto, R. Syntheses of high-valent fac-[$^{99m}$TcO$_3$]$^+$ complexes and [3+2] cycloadditions with alkenes in water as a direct labelling strategy. *Chem. Eur. J.* **2009**, *15*, 633–638. [CrossRef]

49. Braband, H.; Tooyama, Y.; Fox, T.; Simms, R.; Forbes, J.; Valliant, J.F.; Alberto, R. fac-[TcO$_3$(tacn)]$^+$: A versatile precursor for the labelling of pharmacophores, amino acids and carbohydrates through a new ligand-centred labelling strategy. *Chem. Eur. J.* **2011**, *17*, 12967–12974. [CrossRef]

50. Wuillemin, M.A.; Stuber, W.T.; Fox, T.; Reber, M.J.; Brühwiler, D.; Alberto, R.; Braband, H. A novel $^{99m}$Tc labelling strategy for the development of silica based particles for medical applications. *Dalton Trans.* **2014**, *43*, 4260–4263. [CrossRef]

51. Wuillemin, M.A. $^{99m}$Tc-and Re-Based Target Specific Multimodality (Nano)Particles. Ph.D. Thesis, University of Zurich, Zürich, Switzerland, 2018.

52. Nielsen, A.; Bond, A.D.; McKenzie, C.J. N,N-Bis(2-pyridiniomethyl)glycine diperchlorate. *Acta Crystallogr. E* **2005**, *61*, o516–o517. [CrossRef]

53. Kim, W.D.; Hrncir, D.C.; Kiefer, G.E.; Sherry, A.D. Synthesis, crystal structure, and potentiometry of pyridine-containing tetraaza macrocyclic ligands with acetate pendant arms. *Inorg. Chem.* **1995**, *34*, 2225–2232. [CrossRef]

54. Farrugia, L.J. ORTEP-3 for windows-a version of ORTEP-III with a Graphical User Interface (GUI). *J. Appl. Crystallogr.* **1997**, *30*, 565. [CrossRef]

55. Steiner, T. Hydrogen-bond distances to halide ions in organic and organometallic crystal structures: Up-to-date database study. *Acta Crystallogr. B* **1998**, *54*, 456–463. [CrossRef]

56. Crucho, C.I.C.; Baleizão, C.; Farinha, J.P.S. Functional group coverage and conversion quantification in nanostructured silica by $^1$H NMR. *Anal. Chem.* **2017**, *89*, 681–687. [CrossRef]

57. Grundler, P.V.; Helm, L.; Alberto, R.; Merbach, A.E. Relevance of the ligand exchange rate and mechanism of fac-$[(CO)_3M(H_2O)_3]^+$ (M = Mn, Tc, Re) complexes for new radiopharmaceuticals. *Inorg. Chem.* **2006**, *45*, 10378–10390. [CrossRef]

58. Alberto, R.; Ortner, K.; Wheatley, N.; Schibli, R.; Schubiger, A.P. Synthesis and properties of boranocarbonate: A convenient In Situ co source for the aqueous preparation of $[^{99m}Tc(OH_2)_3(CO)_3]^+$. *J. Am. Chem. Soc.* **2001**, *123*, 3135–3136. [CrossRef]

59. Braband, H.; Benz, M.; Tooyama, Y.; Alberto, R. Activation of $[^{99(m)}TcO_4]^-$ by phosphonium cations. *Chem. Commun.* **2014**, *50*, 4126–4129. [CrossRef]

60. Zucchetto, N.; Brühwiler, D. Tuning the aspect ratio of arrays of silica nanochannels. *RSC Adv.* **2015**, *5*, 74638–74644. [CrossRef]

61. Ritter, H.; Brühwiler, D. Accessibility of amino groups in postsynthetically modified mesoporous silica. *J. Phys. Chem. C* **2009**, *113*, 10667–10674. [CrossRef]

62. Brunauer, S.; Emmett, P.H.; Teller, E. Adsorption of gases in multimolecular layers. *J. Am. Chem. Soc.* **1938**, *60*, 309–319. [CrossRef]

63. Ravikovitch, P.I.; Neimark, A.V. Characterization of nanoporous materials from adsorption and desorption isotherms. *Colloids Surf. A* **2001**, *187*, 11–21. [CrossRef]

64. Rigaku Oxford Diffraction. *CrysAlis$^{Pro}$ Software System*; 171.39; Rigaku Oxford Diffraction: Oxford, UK, 2017.

65. Sheldrick, G. A short history of SHELX. *Acta Cryst.* **2008**, *64*, 112–122. [CrossRef] [PubMed]

66. Sheldrick, G. Crystal structure refinement with SHELXL. *Acta Cryst.* **2015**, *71*, 3–8. [CrossRef]

67. Hübschle, C.B.; Sheldrick, G.M.; Dittrich, B. ShelXle: A Qt graphical user interface for SHELXL. *J. Appl. Crystallogr.* **2011**, *44*, 1281–1284. [CrossRef] [PubMed]